

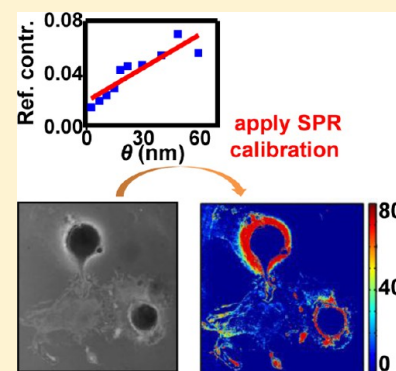
Quantitative Reflection Imaging of Fixed *Aplysia californica* Pedal Ganglion Neurons on Nanostructured Plasmonic Crystals

An-Phong Le,^{†,||} Somi Kang,^{‡,||} Lucas B. Thompson,[†] Stanislav S. Rubakhin,^{†,§} Jonathan V. Sweedler,^{†,§} John A. Rogers,^{†,‡} and Ralph G. Nuzzo^{*,†,‡}

[†]Department of Chemistry, [‡]Department of Materials Science and Engineering, and [§]Beckman Institute for Advanced Science and Technology, University of Illinois at Urbana–Champaign, Urbana, Illinois 61801, United States

S Supporting Information

ABSTRACT: Studies of the interactions between cells and surrounding environment including cell culture surfaces and their responses to distinct chemical and physical cues are essential to understanding the regulation of cell growth, migration, and differentiation. In this work, we demonstrate the capability of a label-free optical imaging technique—surface plasmon resonance (SPR)—to quantitatively investigate the relative thickness of complex biomolecular structures using a nanoimprinted plasmonic crystal and laboratory microscope. Polyelectrolyte films of different thicknesses deposited by layer-by-layer assembly served as the model system to calibrate the reflection contrast response originating from SPRs. The calibrated SPR system allows quantitative analysis of the thicknesses of the interface formed between the cell culture substrate and cellular membrane regions of fixed *Aplysia californica* pedal ganglion neurons. Bandpass filters were used to isolate spectral regions of reflected light with distinctive image contrast changes. Combining of the data from images acquired using different bandpass filters leads to increase image contrast and sensitivity to topological differences in interface thicknesses. This SPR-based imaging technique is restricted in measurable thickness range (~ 100 – 200 nm) due to the limited plasmonic sensing volume, but we complement this technique with an interferometric analysis method. Described here simple reflection imaging techniques show promise as quantitative methods for analyzing surface thicknesses at nanometer scale over large areas in real-time and in physicochemical diverse environments.



1. INTRODUCTION

Quantitative investigations of cell structure and cell-substrate interactions are important in understanding mechanisms and dynamics of cell growth.^{1–7} Two-dimensional optical imaging is widely performed to study structural and biological processes of cells. Bright field microscopy is a standard and extensively used optical imaging technique. It has the limitation, however, of low imaging contrast and resolution.⁸ Phase contrast microscopy (PCM)⁹ and differential interference contrast microscopy^{10,11} have been developed to increase the contrast and resolution of images without cell staining with different dyes. Unfortunately, both methods create distortions around the edges of the sample due to halo effects¹² and require complicated adjustments to the microscope's condenser and phase contrast. Fluorescence microscopy is a tremendously important technique—one well suited to studying specific structures or processes within cells by detecting naturally fluorescent compounds or tagging molecules of interest with fluorophores such as small organic dyes or quantum dots.^{5,13,14} Through careful choice of fluorophores, multiple structures can be tagged and visualized simultaneously, but a primary difficulty of using fluorescent labels is their introduction and detection without altering the physiological and morphological parameters of live cells.^{15–17}

While these two-dimensional imaging techniques provide useful information about cells, their data is ultimately a

projection of a three-dimensional image with a deficiency of information along the z axis. Scanning confocal microscopy^{5,18} and spinning disk confocal microscopy^{19,20} lift this constraint and allow the creation of three-dimensional (3D) images of cells by acquiring in-focus two-dimensional (2D) optical slices from several depths within a sample and then reconstructing a 3D composite image. These methods, while extremely powerful, have inherent limitations that stem from diffraction and fluorescence saturation, and protocols for fluorescently labeling cellular structures often require extensive optimization.²¹ Digital holographic microscopy provides label-free and quantitative phase contrast images by digitally recording the light wavefront from the object under investigation as a hologram and calculating the object images using a numerical reconstruction algorithm.²² Spatial light interference microscopy (SLIM) combines PCM and holography to measure structures and dynamics in cells via interferometry: PCM is able to measure the intrinsic contrast, and holography renders quantitative phase maps.²³ While these techniques are capable

Special Issue: Peter G. Wolynes Festschrift

Received: March 19, 2013

Published: May 6, 2013

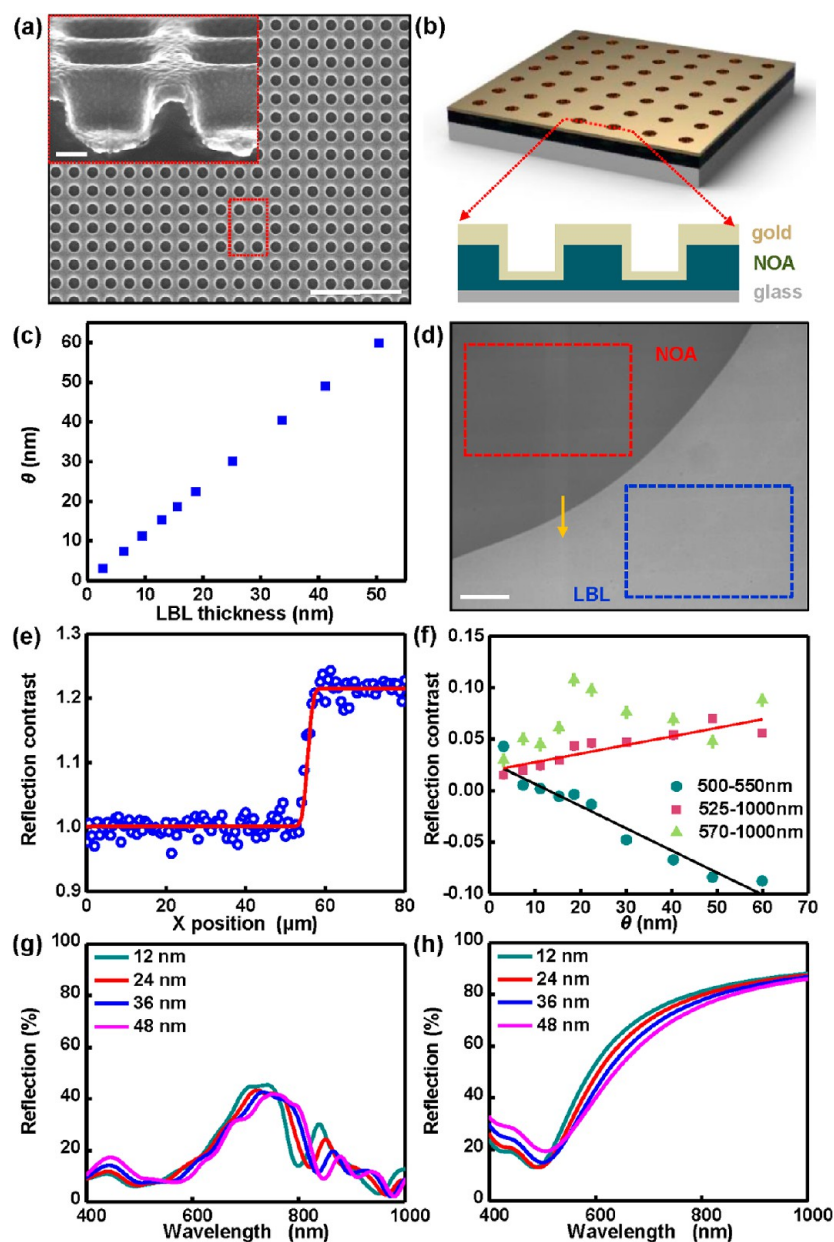


Figure 1. (a) The SEM image of the plasmonic crystal with diameters and periodicities of ~ 460 and 740 nm. The scale bar corresponds to $5 \mu\text{m}$. Inset: Tilted SEM image of red box. The scale bar corresponds to 100 nm. (b) Top: 3D schematic of the plasmonic crystal. Bottom: 2D schematic of cross section of plasmonic crystal (c) Corresponding pairs of thicknesses for polyelectrolyte films and index-corrected material ($n = 1.5$) (θ) determined via ellipsometry. (d) Reflection image (using a $500\text{--}550$ nm bandpass filter) of a polyelectrolyte LBL and photocured polyurethane drop (NOA) on a plasmonic crystal used for the reflection contrast calibration. Average pixel intensities were calculated in the regions marked with red box (NOA region) and blue box (LBL region), and used to determine the reflection contrast calibration. The scale bar corresponds to $100 \mu\text{m}$. (e) Step-edge profile of normalized reflection contrast (NRC; blue circles) along the yellow arrow in panel d and the fitted red curve with a Gaussian width of $1.0 \mu\text{m}$. (f) NRC as a function of index-corrected thickness (θ) using three different bandpass filters: $500\text{--}550$ nm (dark cyan circles), $525\text{--}100$ nm (pink squares), and $570\text{--}1000$ nm (yellow-green triangles). The black line shows the best fit linear regression for the $500\text{--}550$ nm bandpass filter ($\text{NRC} = -0.00224\theta + 0.03183$), and the red line shows that for the $525\text{--}1000$ nm bandpass filter ($\text{NRC} = 0.00085\theta + 0.01872$). The error bars are obscured by the data markers themselves as a result of the large number of pixels (more than $50\,000$) used to determine the value. (g) FDTD calculated reflection spectra for varying thicknesses of polyelectrolyte assemblies on a nanostructured plasmonic crystal. (h) FDTD calculated reflection spectra for varying thicknesses of polyelectrolyte assemblies on flat gold film.

of three-dimensional imaging, they require complex and highly demanding setups and data processing.

An alternative to optical imaging systems, atomic force microscopy (AFM) can be used to directly map the topography of a surface with feature heights ranging from angstroms to micrometers.^{24–26} The relatively long acquisition time needed to collect AFM data is, however, a major drawback to

monitoring dynamics in real time. Live cells, which are soft, can also be physically damaged during data acquisition due to physical contact between the moving AFM tip and the sample. More significantly, though, the interfaces formed by cell-substrate contacts are generally inaccessible to study by AFM.

Surface plasmon resonance (SPR) imaging is a label-free and highly sensitive method for studying interactions occurring

between a substrate and a biological sample. SPRs are coherent oscillations of electron density occurring at the interface of a metal and a dielectric, which generate an evanescent electric field that decays exponentially within ~ 100 – 200 nm from the surface of the metal.^{27–30} The optical sensitivity of SPR to changes in refractive index and layer thickness within the sensing volume has been exploited in biological-sensing, providing both qualitative and quantitative data in real-time without requirements for external labeling.^{31–35} It is particularly well suited for studying the effect of substrate interactions on cellular morphology and growth. SPR-imaging studies have demonstrated both refractive index mapping and thickness profiling of cell-surface contacts.^{36–38} Many current SPR-imaging techniques, however, require relatively complex optical alignment schemes because they utilize a prism to couple polarized light into a flat gold film.^{27,31,35,39}

Nanostructured grating-based systems represent, in principle, a simple platform design for quantitative SPR-imaging, one capable of high spatial resolution arising from the excitation of localized surface plasmon resonances (LSPRs).^{29,40–45} We have previously demonstrated plasmonic imaging with molecular scale sensitivity in white light using nanohole plasmonic crystals fabricated by nanoimprint soft lithography, a common laboratory microscope, and a charge-coupled device (CCD) camera.⁴⁶ The quantitative optical responses of this plasmonic crystal system in air as a function of thickness (up to ~ 90 nm thick of material immediately adjacent to metal surface) were characterized in these earlier studies.⁴²

We extend this method in the present work to the imaging of complex biological surface structures, explicitly treating within finite-difference time-domain (FDTD) theoretical simulations the use of the wavelength dependence as a means to enhance image contrasts and film thickness sensitivities via the quantitative analysis of multispectral plasmonic reflection images collected using bandpass filters. We carried out companion experimental studies using a model full 3D plasmonic crystal with high analytical sensitivity for quantitative imaging in white light, enhancing its responses using multispectral measurements. The multispectral image contrasts were calibrated against polyelectrolyte layer-by-layer (LBL) assemblies with well-defined thicknesses and applied to quantitate the thicknesses of peripheral structures of *Aplysia* pedal neurons cultured and fixed on the surface of a nanostructured plasmonic crystal. We further describe how nonplasmonic optical effects revealed in these multispectral images can be used to extend the described quantitative optical measurements to structural features of a cell that are thicker than the plasmonic sensing volume.

2. EXPERIMENTAL MATERIALS AND METHODS

2.1. Materials. Reagents were used as received without further purification unless otherwise specified. Spin-on-glass (SOG; Accuglass 314) was purchased from Honeywell and was filtered through $0.02 \mu\text{m}$ syringe filters (Whatman Anotop 10) immediately before use. Photocurable polyurethane (NOA 73) was purchased from Norland Products. Polydimethylsiloxane (soft PDMS; Sylgard 184, Dow Corning) was made in a 10:1 ratio of PDMS base with curing agent. Hard PDMS components: poly(25–30% methylhydrosiloxane)-(dimethylsiloxane) (HMS-301), poly(7–8% vinylmethylsiloxane)-(dimethylsiloxane), (VDT-731), platinum divinyltetramethyldisiloxane (SIP6831.1), and (1,3,5,7-tetravinyl-1,3,5,7-tetramethylcyclotetrasiloxane) (7900) were purchased from Gelest.

Manganese chloride tetrahydrate, poly(sodium 4-styrenesulfonate) (PSS, MW = 70,000 g/mol), poly(allylamine hydrochloride) (PAH, MW = 70,000 g/mol), and 4,4'-dithiodibutyric acid (DTBA) were purchased from Sigma-Aldrich. Ultrapure water ($18 \text{ M}\Omega$) was generated using a Millipore Milli-Q Academic A-10 system and used to prepare the polyelectrolyte solutions.

2.2. Plasmonic Crystal Fabrication via Soft Nanoimprint Lithography. Full 3D plasmonic crystals were fabricated using soft nanoimprint lithography as previously reported.^{29,41–45} Briefly, a composite hard-PDMS/soft-PDMS was cast from a patterned photoresist master with an array of nanohole relief structures and used to mold a replica master in SOG. An additional composite PDMS stamp was then cast from the SOG master and subsequently used to fabricate the plasmonic crystals used in this study; a schematic illustration of the nanoimprinting process is presented in Figure S1. A photocurable polyurethane polymer (NOA) was drop cast onto a glass slide, and the second PDMS stamp was pressed into the liquid prepolymer and then exposed to ultraviolet light (UVOCS UV-ozone cleaning chamber) for 5 min to cure the polyurethane. The stamp was peeled away from the patterned polymer structure, and the embossed polymer was cured at 65°C overnight. The replicated nanostructures were a well-defined square array of nanowells with a hole spacing (center to center) of ~ 740 nm, a hole diameter of ~ 460 nm, and a relief depth of ~ 300 nm (scanning electron microscopy (SEM) image of nanoholes is shown in Figure 1a). An adhesion layer (5 nm TiO_2) and a metal layer (32 nm gold) were sputtered onto the relief structure (AJA international, 5 mTorr argon) to complete the plasmonic crystal fabrication.

2.3. Growth of Polyelectrolyte LBL Assemblies on Gold Films. Polyelectrolyte LBL assemblies were grown on the surface of the plasmonic crystals and on gold-coated silicon wafers following previously reported procedures.^{42,47} A small drop of NOA was applied to one corner of the plasmonic crystal and cured to block a region of the plasmonic crystal from adsorption of the polyelectrolyte film. Carboxyl-terminated self-assembled monolayers were formed on the gold film surface by immersing the substrate in ethanolic solutions of DTBA (33 mM) for 24 h, after which the gold films were rinsed thoroughly with ethanol and dried with nitrogen gas. The thiol end-group of DTBA helped to anchor itself on the gold surface, and the negatively charged carboxylic acid end-group served as the initial layer to electrostatically attract the positively charged PAH. Layers of PAH and PSS were alternately adsorbed onto the surface to build up the polyelectrolyte assembly. The substrates were immersed in a PAH solution (3 mg PAH/mL in water, $\text{pH} = 8.0$) for 5 min, rinsed thoroughly with water, and dried with nitrogen gas. The substrate was then immersed in a PSS solution (3 mg PSS/mL in 1 M MnCl_2 , $\text{pH} = 2.0$) for 90 s, rinsed with water and dried with nitrogen gas. Each round of polyelectrolyte deposition consisted of the adsorption of one PAH and one PSS layer, and reflection images and ellipsometry measurements were collected after each round of polyelectrolyte depositions.

2.4. Ellipsometry of Polyelectrolyte LBL Assemblies. The thicknesses of polyelectrolyte LBL assemblies grown on gold-coated pieces of silicon were measured using a Woollam VASE spectroscopic ellipsometer using 50° and 70° incident angles; data were collected over a wavelength range of 400 – 900 nm. The polyelectrolyte layer was modeled as a Cauchy material with parameters $A_n = 1.61$, $B_n = 0.01$, $C_n = 0$ such that

the modeled refractive index at 630 nm was 1.635.^{42,47} The equivalent thickness for a refractive index-corrected material corresponding more closely to a protein film was modeled from the spectroscopic ellipsometry data by substituting the polyelectrolyte layer in the model for a layer modeled as a Cauchy material with parameters $A_n = 1.47$, $B_n = 0.01$, $C_n = 0$ corresponding to a refractive index $n = 1.495$ at 630 nm.^{48,49}

2.5. Cell Culture of *Aplysia californica* Pedal Ganglion Neurons. Sea slug *Aplysia californica* (100–300 g) were supplied by the National Resource for *Aplysia* (Miami, FL) and kept in circulated, aerated seawater at 14 °C. Prior to dissection, the animals were anesthetized by injection of isotonic magnesium chloride solution into the body cavity (~30–50% of body weight). Individual *Aplysia* pedal neurons were isolated after incubation in artificial seawater (ASW; (in mM) 460 NaCl, 10 KCl, 10 CaCl₂, 22 MgCl₂, 26 MgSO₄, and 10 HEPES, pH 7.7) supplemented with proteases (1% type XIV, Sigma-Aldrich) at 34 °C for 60–120 min.^{50,51} *Aplysia* neurons can be grown on a variety of substrates assuming correct surface chemistry is present and had no difficulties growing on the plasmonic crystal surface.^{52–54} A poly-L-lysine layer was formed on the plasmonic crystal surface, and the cells were mechanically isolated in ASW, transferred onto the plasmonic crystal surface immersed in ASW supplemented with antibiotics (ASW containing 100 units/ml penicillin G, 100 mg/mL streptomycin, and 100 mg/mL gentamicin, pH 7.7) and left to attach and grow overnight at room temperature. Six to eight pedal ganglion neurons were sparsely cultured on the plasmonic crystal surface at a time. Cells were fixed by addition of 1 mL of 4% paraformaldehyde to 3 mL of ASW antibiotic culture media and occasional stirring for 30s, removal of 1 mL of the solution, addition of another 1 mL of the 4% paraformaldehyde solution and exposure for 30 s, followed by the removal of all solution. After removal of the fixation solution, the cells were rinsed with deionized water and dried.

2.6. Reflection Mode Plasmonic Imaging. Reflection mode images of both the polyelectrolyte films and cells cultured on the plasmonic crystal surface were obtained using an Olympus AX-70 upright microscope with a halogen light source and a 20×, 0.40 NA objective lens. A frosted glass filter was placed immediately in front of the light source to homogenize the incident illumination. The plasmonic crystal was turned upside-down so that light would be incident first on the glass substrate of the plasmonic crystal and then propagate to the nanostructured metal surface. Bandpass filters (500–550 nm, 525–100 nm, 570–600 nm, 570–1000 nm, and 610–700 nm) were purchased from Omega Optical and inserted in front of the microscope camera. Images were captured using an Optronics Magnafire CCD camera (1280 × 1024 array of pixels, each pixel 6.7 × 6.7 μm). The halogen lamp intensity was varied to control the overall exposure. Grayscale images were acquired using individual exposure times of 750 ms with 15 consecutive images averaged together. Image processing and contrast calibration was performed using Matlab and ImageJ.

Vignetting in the reflection images was corrected using images of a silver mirror acquired with each bandpass filter. A Gaussian blur (100 pixel radius) was applied to the reference mirror image to remove blemishes and debris in the image, and the reference image was normalized by dividing each pixel by the averaged pixel intensity in the image.⁵⁵ Vignetting in the polyelectrolyte layer and cell images was corrected using a pixel-by-pixel division of the experimental image by the blurred

mirror reference image obtained with the corresponding bandpass filter.

2.7. AFM and SEM of Cells on Plasmonic Crystals. AFM height profiles of *Aplysia* neurons cultured on the surface of the plasmonic crystal were measured using an Asylum Research MFP-3D atomic force microscope operated in tapping mode. Analysis of the data, including the fast Fourier transform (FFT) filtering, was performed using IgorPro. Scanning electron microscope (SEM) images of *Aplysia* neurons cultured on plasmonic crystal were acquired using a JEOL 6060-LV scanning electron microscope operated under high vacuum. A thin layer of Au/Pd was sputtered onto the plasmonic crystal and *Aplysia* neuron after all other analyses were completed to make the sample electrically conductive for SEM imaging.

2.8. FDTD Simulations of Plasmonic Nanostructures. 3D FDTD simulations were carried out to model the zero-order reflection spectra (with light normally incident on the glass substrate) and their dependence on the polyelectrolyte layer thickness. The unit cell grid spacing was 4 nm in all three dimensions, with a total unit cell size of 187 × 187 × 600 grid points. The unit cell geometry defined a gold nanohole in the x – y plane with a 740 nm center-to-center hole spacing, 456 nm hole diameter, 292 nm relief depth, 32 nm Au film on the top surface of the plasmonic crystal, 12 nm Au film conformally coating the nanohole sidewalls, and 12 nm Au film on the bottom of the nanoholes. Periodic boundary condition in x and y axis generated an infinite square array, and uniaxial perfectly matched layers were incorporated on the top and bottom surfaces of the unit cell to minimize the effects of unintended reflection from the domain boundaries. The frequency dependent dielectric constant of gold was modeled using previously reported parameters from a Drude plus two-pole Lorentzian model.³⁶ The refractive indices of NOA, polyelectrolyte, refractive index-corrected material, and air were taken to be 1.56, 1.64, 1.50, and 1.00, respectively.

3. RESULTS AND DISCUSSION

3.1. Plasmonic Crystals and Biological System Model.

We examined a model biological system, pedal ganglion neurons isolated from *Aplysia californica* central nervous system and cultured on a plasmonic crystal. We provide a quantitative analysis of the cell peripheral structural features. Specifically, residual structures associated with the growth cones and cytoplasmic extensions mediating neurite development using contrasts observed in multispectral images. The analytical method described here offers a proof of principle for the analytical method that can be applied more broadly in reflection mode imaging studies of complex biological systems. We conducted these studies using a full 3D plasmonic crystal (Figure 1a,b) that past work demonstrated possesses molecular sensitivity in imaging mode analyses performed in white light.⁴⁶ Work was done on the square array of embossed nanoholes (460 nm diameter, 300 nm depth, 740 nm pitch) conformally coated with 32 nm of Au (Figure 1a). We begin the discussion by establishing first the means by which plasmonic crystal image contrasts can be measured and quantitatively interpreted within an experimentally validated theoretical model. We follow this by showing an exemplary application of measurements made of plated cells that were fixed after various periods of growth in culture.

3.2. Reflection Imaging Contrast Calibration. Polyelectrolyte films comprised of PAH and PSS were assembled on the

surface of the plasmonic crystal via LBL self-assembly.^{42,47} The films were measured to calibrate the reflection contrast changes associated with changes in film thickness. Spectroscopic ellipsometry was used to determine the thickness of dried polyelectrolyte films, which were simultaneously deposited onto gold-coated silicon wafer pieces under identical conditions. The results showed that the thickness of the polyelectrolyte assemblies increases by 3.02 ± 0.38 nm for each PAH/PSS deposition step.

The optical response of the plasmonic crystal is influenced by the local refractive index environment and the thickness of the dielectric above the metal surface. For this reason, imaging mode contrast calibrations made using LBL films may complicate quantitative analyses of biological materials due to their markedly different optical properties: the refractive index (n) of the polyelectrolyte is ~ 1.64 ^{42,47} and that for a biological specimen being more typically is ~ 1.35 – 1.5 .^{48,49} Ellipsometry, which is sensitive to both layer thickness and refractive index, was used to measure the thicknesses of the polyelectrolyte films and to determine the thickness required for a film with a refractive index more appropriate for biological materials with high organic content ($n \sim 1.50$) to exhibit similar ellipsometric behavior (the chosen modeling parameters are included in the Experimental Materials and Methods section). For clarity, we operate with a refractive index-corrected thickness for the biological samples (θ), which corresponds to that thickness determined through ellipsometric modeling. Figure 1c presents the corresponding pairs for polyelectrolyte and index-corrected thicknesses.

The validity of the ellipsometric thickness reference conversion was evaluated using FDTD calculations. Figure S2 presents the calculated reflection spectra for a plasmonic crystal coated with a conformal layer of either polyelectrolyte or the equivalent index-corrected material representing the biological material of fixed cells. These data clearly demonstrate the suitability of a single optical data set from the polyelectrolyte LBL assemblies as a calibration reference. The nearly identical reflection spectra show excellent correspondence between the optical properties of the polyelectrolyte and the index-corrected material. The small discrepancies between the spectra likely stem from limitations in the computational model as the equivalent index-corrected thickness was not an exact multiple of the modeled grid spacing of 4 nm.

Reflection images of polyelectrolyte LBL films deposited on the plasmonic crystal surface were acquired with bandpass filters inserted immediately in front of the CCD camera. The plasmonic crystal was imaged from the reverse side, and a representative image is presented in Figure 1d. To correct for variation in illumination intensity between images, a drop of photocurable polyurethane (NOA) was deposited and cured on one corner of plasmonic crystal surface. This NOA-covered region (labeled as NOA in Figure 1d) was blocked from subsequent polyelectrolyte depositions, creating a region where the surface refractive index profile remained constant. The region marked LBL in Figure 1d denotes the area where the polyelectrolyte was deposited. The dot boxes drawn in Figure 1d illustrate where the average pixel intensity was calculated for the NOA and LBL regions. The normalized pixel values for the LBL region in images taken of each LBL deposition were scaled according to the following relationships. In the first, the average pixel intensity values for the polyelectrolyte-free NOA regions in all images were equated according to eq 1:

scaled LBL average

$$= [\text{image LBL average}] \times \frac{[\text{reference NOA average}]}{[\text{image NOA average}]} \quad (1)$$

The normalized reflection contrast was calculated using the scaled average pixel intensity of the LBL regions according to eq 2:

normalized reflection contrast

$$= \frac{[\text{scaled LBL average}] - [\text{reference LBL average}]}{[\text{reference LBL average}]} \quad (2)$$

where the reference average is defined as the average pixel intensity of the reflection image for the plasmonic crystal before the LBL deposition. Use of the scaled LBL average pixel values corrects for differences in illumination intensity between images, while the normalized reflection contrast expresses the relative reflection contrast change of the LBL region as compared to the reference LBL average pixel intensities. This normalized reflection contrast value may be positive or negative, corresponding to reflectivity higher or lower than the reference condition.

To demonstrate the contrast difference between the polyelectrolyte and polyelectrolyte-free regions and to estimate the lateral resolution of the optical system, Figure 1e shows the step-edge profile for the normalized reflection contrast along the yellow arrow shown in Figure 1d. A step function was convolved with a Gaussian function and iterated in width to match the observed behavior of the reflection contrast.⁴¹ The resultant fit (red line, as presented in Figure 1e) shows that the data can be well modeled with a limiting lateral resolution of $1.0 \mu\text{m}$. This value is only slightly larger than the spatial resolution limit of the microscope optics and camera at this magnification, $\sim 0.67 \mu\text{m}$.

While the center-to-center spacing between holes is ~ 740 nm, depending on the optical alignment, a single pixel in the image of the plasmonic crystal may overlap part of one or several nanoholes. It is reasonable that the reflectivity may not be identical between the top and bottom surfaces of the nanohole, and the pixel intensity could vary somewhat due to differences in nanohole coverage. All the same, we noted no particular patterns appearing in histograms of the pixel intensities in the calibration images.

The normalized reflection contrast (NRC) change as a function of refractive index-corrected thickness is presented in Figure 1f. The reflection contrast becomes more negative as the surface layer thickness (θ) increases when a 500–550 nm bandpass filter is used, while the reflection contrast becomes more positive when imaged using a 525–1000 nm bandpass filter. These experimental data demonstrate a “contrast inversion” in which the reflection intensity changes increase or decrease depending on the wavelengths used. Because a simple linear regression is more adequate to mathematically interpret this experimental behavior, linear regressions were calculated for both wavelength ranges: $\text{NRC} = -0.00224\theta + 0.03183$ for the 500–550 nm bandpass filter (black line in Figure 1f), and $\text{NRC} = 0.00085\theta + 0.01872$ for the 525–1000 nm bandpass filter (red line in Figure 1f). More complex reflection contrast behaviors were observed at other wavelength ranges. Using a 570–1000 nm bandpass filter, for example, a nonmonotonic dependence is seen in which the reflection

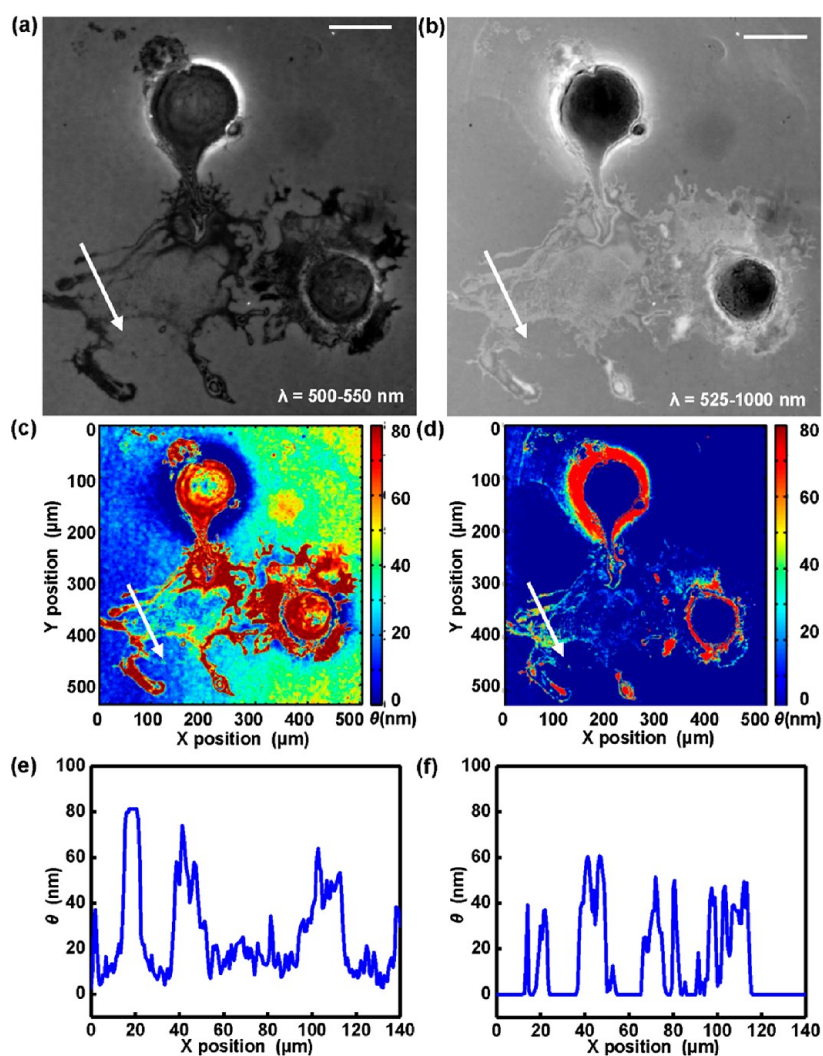


Figure 2. (a,b) Reflection images of an *Aplysia* neuron cultured on a plasmonic crystal surface acquired using (a) 500–550 nm bandpass filter and (b) 525–1000 nm bandpass filter. The scale bar in panels a and b corresponds to 100 μm . (c,d) Index-corrected thickness (θ) calibrations applied to reflection images of an *Aplysia* neuron cultured on a plasmonic crystal acquired using (c) 500–550 nm bandpass filter and (d) 525–1000 nm bandpass filter. The z-scale for image is restricted to the plasmonic sensing volume (0–80 nm). (e,f) Height profiles (along the white arrow) of the quantitative reflection image acquired using (e) 500–550 nm bandpass filter and (f) 525–1000 nm bandpass filter.

contrast initially increases as the surface layer thickness increases but then reverses and begins to decrease as the coverage was further incremented. This complexity is attributed to that of the underlying surface plasmon modes and their changes in response to changes in the refractive index profile of the adsorbed material on the plasmonic crystal surface.

Additional FDTD calculations were performed to determine changes in the optical responses of the plasmonic crystal with increasing polyelectrolyte thickness. Figure 1g presents the theoretically calculated reflection spectra for a plasmonic crystal of the experimental geometry as the thickness of polyelectrolyte was changed. These spectra demonstrate a complex behavior akin to that seen in the reflection imaging contrast calibrations. Some wavelength ranges (e.g., ~ 675 – 770 nm) exhibit a decrease in reflectance with thicker polyelectrolyte films while the opposite trend is observed at other wavelength ranges (e.g., ~ 770 – 820 nm). These trends are similar to those seen in experiment.

For comparison, the simulated reflectance spectra for polyelectrolyte films on flat gold surfaces are presented in Figure 1h. Above $\sim 530 \text{ nm}$, the reflectance intensity decreases

nearly monotonically as the polyelectrolyte layers thickness increases, although the magnitudes of the reflectance changes do exhibit a dependence on wavelength. This flat film modeling accounts for Fresnel effects associated with light interacting with and passing through boundaries between layers with different refractive indices but otherwise lack plasmonic properties. The absence of a wavelength-dependent “contrast inversion” for this flat film akin to that observed experimentally points toward SPRs as the origin of the latter effects.

It is important to note that the results presented in Figure 1g and Figure 1h were obtained from simulations in which the illumination was normally incident to the surface. The reflection images obtained experimentally used an objective lens with a numerical aperture of 0.40, corresponding to a cone of illumination with a maximum angle of $\sim 23^\circ$. This is significant because the spectral properties of the plasmonic crystal are known to depend on illumination angle.⁴⁰ While the computational modeling performed here offers insight into the complexity behind the observed reflection behavior, a more complete theoretical understanding will require simulations that

incorporate those oblique illumination angles, which is not currently possible within our FDTD code.

3.3. Reflection Imaging of Fixed *Aplysia* Pedal Ganglion Neurons on Plasmonic Crystals. To explore the quantitative features of SPR-based reflection imaging of a complex biological specimen, *Aplysia* pedal ganglion neurons were cultured on the surface of a plasmonic crystal (Figure 2). Figure 2a,b presents reflection images of a representative fixed neuron cultured on a nanostructured plasmonic crystal surface, while Figure S3a,b presents images of a cell cultured on a flat gold surface. A visual comparison of the images collected using a 500–550 nm bandpass filter (Figure 2a and Figure S3a) and a 525–1000 nm bandpass filter (Figure 2b and Figure S3b) clearly reveals differences in contrast, including its inversion, in a manner predicted by the computational modeling. The peripheral regions of the fixed neurons on flat gold appear darker than the surrounding area in both the 500–550 nm and 525–1000 nm images, while the analogous regions of the cell grown on the plasmonic crystal show an inversion in contrast where the peripheral region appears darker than the surrounding area in the 500–550 nm image but lighter than the surrounding area in the 525–1000 nm image.

These fixed neurons have features that range in thickness from tens of nanometers to several micrometers. As surface plasmon effects are generally sensitive to refractive index profile changes only within ~ 100 – 200 nm from the metal surface, many of the features seen in the images of Figure 2 must have other origins. The neuron's body on the plasmonic crystal (especially the several tens of micrometers thick regions) appears dark and possesses circumferential bright fringes in the reflection images. These are likely the result of a convolution of various optical phenomena, including light absorption, reflection, and scattering by cellular structures; surface plasmon-mediated reflection; and interference effects. To highlight the plasmonic resonance phenomena manifested in the images of Figure 2, we focus only on those features whose dimensions are within the range where the linear regression of optical response as a function of thickness is valid⁴² (i.e., ~ 80 nm from the surface).

The calibration between reflection contrast and index-corrected thickness presented in Figure 1f were applied to the reflection images shown in Figure 2a,b to determine the thicknesses of the regions of the fixed *Aplysia* pedal neurons behaving as thin films. The normalized reflection contrast was calculated pixel-by-pixel in the cell image using an empty area with no apparent features immediately adjacent to the cell as the reference reflection. The normalized reflection contrast was then transformed mathematically to an index-corrected material thicknesses value using the appropriate regression equation corresponding to the bandpass filter used to acquire the original image. These thickness-transformed cell images are presented in Figure 2c (for the 500–550 nm bandpass filter) and Figure 2d (for the 525–1000 nm bandpass filter).

In calculating the thickness transformations, the normalized reflection contrast values were restricted to θ lying between 0 and 80 nm. Pixel values outside of this range were truncated, resulting in regions of the image being saturated at either the minimum or maximum reflection contrast value. Because the soma has a thickness significantly larger than the plasmonic sensing volume, the thickness estimates of these regions are clearly invalid. Therefore, the analysis performed in this work focuses instead on the thinner neurite outgrowths and growth cone regions, which are arguably more interesting in the study

of cell growth on the substrate. Images from both wavelength regions reveal a sparse film of material in this region with a thickness of ~ 30 nm and string-like filaments with thicknesses of ~ 60 nm. We describe origins for these features in sections that follow.

We note that “empty” regions in the image (with no apparent cell structures) actually have a thin film of poly-L-lysine, which had been applied to the plasmonic crystal surface to improve the biocompatibility of the substrate. The contributions of this poly-L-lysine layer to the estimated thickness can be neglected, however, because its thickness is accounted for when calculating the normalized reflection contrast.

The reliability of the thickness evaluation protocol can be evaluated via the self-consistency of the estimates of film coverage obtained using different bandpass filters. Figure 2e,f demonstrates identical thickness profiles (θ) along the white arrows on cell images obtained using the 500–550 nm and 525–1000 nm bandpass filters, respectively. The effect of truncating the contrast values in the image prior to applying thickness transformation is particularly apparent in the line profile for the 525–1000 nm image (Figure 2f), where many pixels were assigned a thickness of zero. Despite the truncation in the 525–1000 nm image, good agreement is observed for the height of the filament feature at position $X \sim 40 \mu\text{m}$ which both wavelength ranges assign a thickness of ~ 60 nm. Good correspondence is also observed for the feature at $X \sim 110 \mu\text{m}$ where the surface feature thickness is approximately ~ 50 nm. However, the agreement between the two images is poorer for features with smaller values; for example, small features were not observed in the 500–550 nm image as in the 525–1000 nm image between $X \sim 50$ – $90 \mu\text{m}$. This discrepancy may result from the relatively coarse linear regressions applied to the calibration imaging data, which may underestimate or overestimate the contrast change in particular thickness ranges. Using a more finely grained regression analysis or more complex mathematical fits would be expected to yield improved consistency between wavelength regions. Alternatively, as discussed in sections that follow, multispectral image contrasts can be calculated from the component bandpass filter data that provide greatly enhanced capabilities for quantitative imaging.

3.4. AFM Height Profiles of Fixed Cell Features. In addition to comparing profiles measured using different bandpass filters, AFM imaging was performed as an independent verification of the height profiles of the fixed neuron cells structures calculated using data from reflection plasmonic imaging. Representative AFM data are presented in Figure 3a, with a three-dimensional representation of the AFM data shown in Figure 3b. These images reveal a periodic modulation that arises from the underlying nanohole array that comprises the plasmonic crystal. The periodic modulation from the underlying substrate is not observed in the reflection images because the individual nanoholes (~ 460 nm in diameter) are smaller than the length scales resolved by the camera at this magnification (~ 670 nm) and the likely “smearing” due to the comparable length scale of the LSPRs that the plasmonic crystal supports.^{28,29}

The periodic modulation in the AFM images resulting from the plasmonic crystal topography adversely affects the analysis of the thicknesses of cellular features on the surface. To overcome this, the periodic oscillations were filtered out using an FFT of the image where all but the lowest frequency components were removed. A 3D projection of the FFT filtered

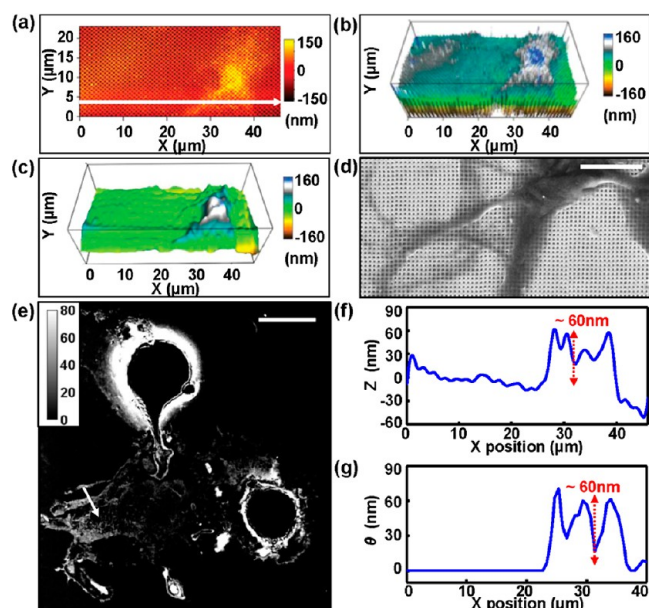


Figure 3. (a) AFM image of an *Aplysia* neuron cultured on a plasmonic crystal showing periodic structures on the surface due to the underlying plasmonic nanostructure. (b) 3D projection of the original AFM data of panel “a” showing periodic topological features on the neuronal surface. (c) 3D projection of AFM data of panel “a” after FFT filtering to remove plasmonic nanostructure contribution. (d) SEM image of a portion of an *Aplysia* neuron cultured on plasmonic crystal showing the nanostructured surface underneath the cell structures. The scale bar corresponds to 100 μm . (e) Index-corrected thickness (θ) calibration applied to the reflection image of an *Aplysia* neuron cultured on a plasmonic crystal acquired using 525–1000 nm bandpass filter. The scale bar corresponds to 100 μm . (f) AFM height profile along the white arrow drawn in panel “a”. (g) Reflection contrast height profile along the white arrow drawn in panel “e”.

data is presented in Figure 3c. There is a loss resolution that occurs as a result of the FFT filtering. A scanning electron micrograph of a similar fixed cell is presented in Figure 3d. This image shows that the thinner cell outgrowth regions conform, at least partially, to the plasmonic crystal’s surface topography, while thicker layers appear to be less strongly affected, with structured features similar to those seen in the AFM data.

A comparison of height profiles is presented in Figure 3f for the AFM image and in Figure 3g for the plasmonic reflection image. These profiles were taken from the same cell area represented by the white arrows superimposed on the AFM image in Figure 3a and the reflection image in Figure 3e. Comparing the two height profiles reveals a marked correspondence in the thickness estimates of the filament structures at $X \sim 30 \mu\text{m}$ in the AFM profile (Figure 3f) and at $X \sim 30 \mu\text{m}$ in the reflection image profile (Figure 3g); both methods assign the feature a thickness of $\sim 60 \text{ nm}$. These AFM data thus provide independent confirmation of the thicknesses estimated using the plasmonic reflection contrast calibrations and of the estimated refractive index of the fixed cell material. The latter value, being higher than the refractive index of live cell components (where $n \sim 1.35 - 1.41$), reflects the loss of water from the materials present in the fixed cell.

3.5. Increased Image Contrast through Wavelength Combination. A CCD camera was used as the imaging detector in this work, which integrates the photon flux across the accessible wavelength range to report pixel intensity. Reflectivity changes in the sample result in changes in the

photon flux and are interpreted as reflectance changes in the image, and an increase in the number of photons at one wavelength within that accessible range of reflected light can be offset by a decrease in photons at a different wavelength within that range. The integrative nature of the CCD camera can ultimately result in reduced image contrasts if the wavelengths used overlap spectral regions with opposite contrast behavior (where the reflectance increases at one wavelength but decreases at another). Bandpass filters allow these spectral regions to be isolated from one another and analyzed separately in a form of quasi-hyperspectral imaging, albeit one with relatively coarse wavelength control. By identifying wavelength regions where the reflection contrast exhibits opposite behaviors and imaging these regions separately, recombination of the data from those wavelength regions can be used to restore or even enhance the contrast.

Figure 4a shows reflection contrast calibration curves obtained using 570–600 nm (yellow-green triangle) and 570–1000 nm (pink square) bandpass filters. Due to the wavelength overlap between the two filters, the reflection behavior between 570 and 600 nm is included in (and convolved within) the optical data collected over the 570–1000 nm wavelength range. These calibration curves indicate that the reflection contrast decreases at θ greater than $\sim 20 \text{ nm}$ in both wavelength ranges, but the contrast decreases obtained using the 570–1000 nm filter are not as pronounced as those found in the 570–600 nm wavelength range. This indicates that the reflection must tend to increase for thicker θ at wavelengths between 600 and 1000 nm in order to offset the contrast decreases that occur over the 570–600 nm range. Most interestingly, the 570–1000 nm data show a larger increase in reflection contrast for thinner θ (up to $\sim 20 \text{ nm}$) than is seen in the 570–600 nm data. It can be concluded as a result that the contrast scaling seen over the 570–600 nm and 600–1000 nm ranges are, in fact, opposite in sign. This provides a means to enhance the overall imaging contrast by recombining images captured over these different wavelength ranges.

The wide spectral response of the camera is needed in order to properly combine the calibration images obtained using different bandpass filters into a single composite calibration curve. The spectral response of the CCD detector is not equal across all wavelengths; its sensitivity peaks between 500 and 520 nm and then decreases with increasing wavelength of the light (as shown in Figure S4).⁵⁶ The 570–600 nm bandpass filter covers only $\sim 7\%$ of the wavelength range between 570 and 1000 nm but accounts for $\sim 18\%$ of the total sensitivity. Thus it results that the contributions of the 570–600 nm wavelength range to the overall image contrast are disproportionately larger relative to the size of the bandpass wavelength range. With consideration of the spectral sensitivity of the CCD camera, the individual images made using the 570–600 nm and 570–1000 nm bandpass filters were weighted by the total integrated sensitivity of camera over the specific wavelength range and combined according to eq 3:

$$\text{composite image} = [([570 - 1000 \text{ nm}] \times 147.75) - 2 \times ([570 - 600 \text{ nm}] \times 26.55)]/147.75 \quad (3)$$

The value of 147.75 originates from the total integrated sensitivity from 570 to 1000 nm (green + pink area) presented on the spectral sensitivity plot in Figure S4, while the 26.55 value is the integrated sensitivity from 570 to 600 nm (green area) in Figure S4. The image data from the 570–600 nm

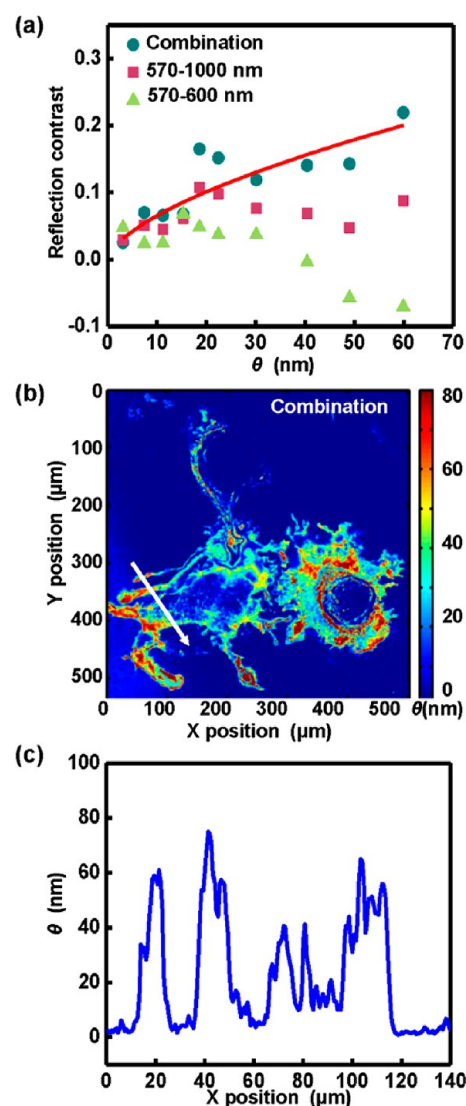


Figure 4. (a) Normalized reflection contrast calibration curves as a function of index-corrected thickness (θ) for fixed cell acquired using bandpass filters: 570–600 nm (yellow green triangles), 570–1000 nm (pink squares), and a combination of the 570–600 nm and 570–1000 nm data (dark cyan circles). A power law regression was applied to the combination calibration curve (red curve, $\text{NRC} = 0.01565\theta^{0.6323}$). (b) Wavelength combined (570–600 nm and 570–1000 nm) reflection contrast calibration applied to wavelength combined image of an *Aplysia* neuron cultured on a plasmonic crystal. (c) Height profile along the white arrow drawn on panel “b”.

wavelength range was subtracted twice in this analysis (via a factor of 2 in the formula above): the first subtraction removes its contribution from the data collected over the entire 570–1000 nm wavelength range, and the second subtraction restores its contribution but with an inverted sign. The resultant image was then used to calculate the normalized reflection contrast as described previously, and the combined contrast calibration results are plotted as the dark cyan circles in Figure 4a. It is readily apparent that the overall reflection contrast increases across the range of index-corrected material thicknesses (θ) examined. A power law regression was applied to model the combined calibration curve, with a best fit of $\text{NRC} = 0.01565\theta^{0.6323}$.

This composite calibration curve was applied to images of the fixed *Aplysia* neurons on the plasmonic crystal (which had

been combined in a similar manner), and the resultant thickness estimates are presented in Figure 4b. The thickness profile in Figure 4c (along the white arrow shown in Figure 4b) shows good agreement with those produced using the 500–550 nm and 525–1000 nm calibration curves (in Figure 2e,f, respectively). The smaller features lying between $X \sim 50$ – $90 \mu\text{m}$, which were not observed in the 500–550 nm image, are clearly resolved in the combination reflection image. These results show the efficacy of combining images acquired in a multispectral form to increase contrast and sensitivity in the resultant image.

3.6. Quantitative Thickness Estimates from Non-plasmonic Optical Effects. While the thickness calibration methods demonstrated here rely on the sensitivity of SPR to changes in the refractive index profile at and near the metal surface, the reflection images also contain other areas of the cell with thicknesses significantly greater than the range of the surface plasmons’ evanescent electric field. Additional and quantitatively useful nonplasmonic optical effects are present in these regions of the image. These include Fresnel reflections from interfaces between materials with different refractive indices along with light scattering and absorption by cellular components. The region boxed in red on the cell image presented in Figure 5a (acquired using a 500–550 nm bandpass filter) highlights a notable nonplasmonic optical effect seen in the reflection image. Rotated and magnified views of this region acquired using 500–550 nm, 570–600 nm, and 610–700 nm bandpass filters are presented in Figure 5b, respectively. These images reveal alternating light and dark bands moving from the lower left tip toward the upper right. The size and position of these band changes depending on the particular bandpass filter used.

These alternating intensity bands represent a thin film interference effect (referred to as Newton’s rings) arising from constructive and destructive interference from light reflected within a resonant cavity formed by the top and the bottom surfaces of the cell structure. The number and position of these bright and dark regions are functions of the wavelengths of light being imaged and the cavity length (cell thickness) required to produce the resonant conditions. Since the wavelengths of light being imaged are known, the thin film interferences provide an additional method to quantitatively estimate the thicknesses of thin film structures presented in the sample. The resonant cavity length was estimated for the second band indicated in the 500–550 nm image (in Figure 5b) using the extreme ends of the range of wavelengths and incident angles (0° and 23.6°) along with the previous estimate of the refractive index ($n \sim 1.5$). The convolution and overlap of different wavelengths with different illumination angles predict a range of cavity thicknesses lying between ~ 300 – 400 nm as being capable of producing constructive interference at the location highlighted in 500–550 nm image (Figure 5b). Further details are included in the Supporting Information.

AFM measurements were made to independently evaluate the latter thickness estimate. A representative FFT filtered AFM image is presented in Figure 5c, and a height profile along the blue arrow in Figure 5c is shown in Figure 5d. The thickness revealed by AFM data is between 300 nm and 400 nm, in good agreement with the thickness analysis for the data in Figure 5b. This interferometric thickness calculation is a simple complement to the surface plasmon-based measurements, capable of measuring surface films thicker than the plasmonic sensing volume without prior calibration. However,

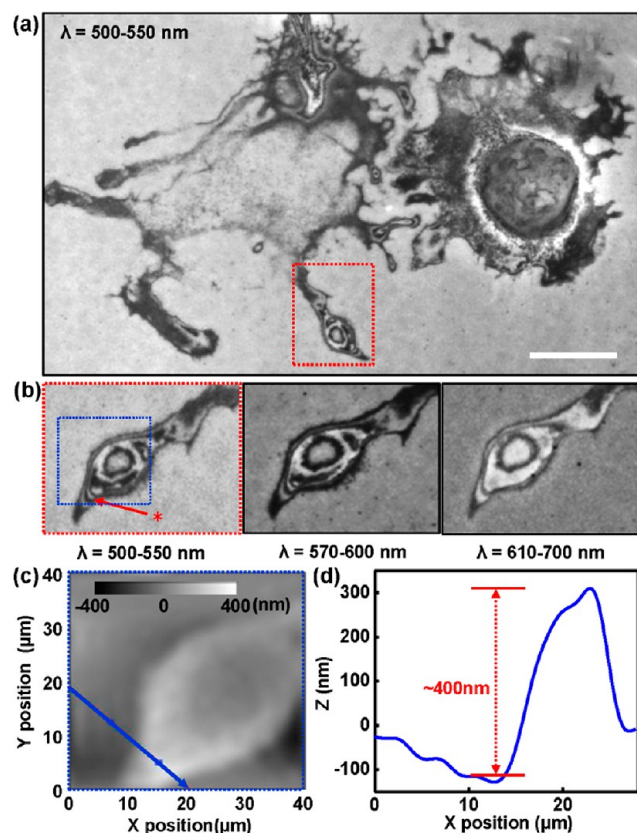


Figure 5. (a) Reflection image of *Aplysia* neurons cultured on a plasmonic crystal acquired using a 500–550 nm bandpass filter. The scale bar corresponds to 100 μm . (b) Rotated and magnified images of the region in the red box in panel “a” acquired using 500–550 nm (left), 570–600 nm (middle), and 610–700 nm (right) bandpass filters. Based on interferometric estimates, the region indicated by the red asterisk and arrow in panel “b” is \sim 330–400 nm thick. (c) FFT filtered AFM image of the *Aplysia* neuron structure displayed in Figure 5 (corresponding to the blue box in panel “b”). (d) AFM height profile along blue arrow drawn in panel “c”.

the thickness range estimates can become very broad when applied to images acquired using large wavelength ranges, and the nature of the microscope objectives themselves results in a range of thicknesses capable of producing constructive or destructive interference at a location (even under monochromatic illumination). The minimum thickness required to observe thin film interference effects are one-half of the wavelength (or one-fourth if reflection from the upper surface results in a 180° phase shift). Even for 400 nm illumination at normal incidence, this corresponds to a minimum thickness of 100 nm—coincidentally, the upper limit for quantitative thickness measurements using plasmonic calibrations. While these considerations constrain the use of thin film interference effects to quantitate material thicknesses, they also suggest possibilities for a synergistic integration of both methods of analysis.

3.7. Inferences Regarding Cell Structures Observed on Plasmonic Crystals. The growth and extension of neuritis from the *Aplysia* pedal ganglion neuron body begins with the emergence of growth cones.⁵⁷ The growth cone is defined by a thicker central region, where vesicles and microtubules can be found, and a surrounding thinner “veil” composed of lamellipodia and filopodia.^{57–59} As the cell matures, materials in the peripheral regions are resorbed as the neurite thickens

and rounds,^{57,60} and it is likely that quantitative analysis of reflection images of neuronal cell structures at different developmental stages might help to elicit new understandings of the neurite outgrowth process.

The images presented in Figure 6 illustrate this notional point, showing fixed *Aplysia* pedal ganglion neurons having

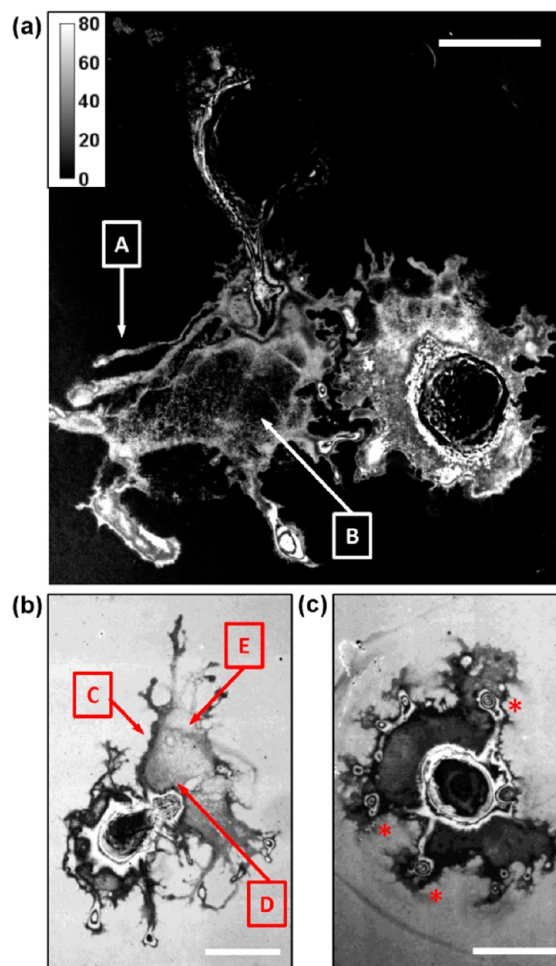


Figure 6. (a) Thickness calibration applied to combined wavelength (570–600 nm and 570–1000 nm) image of *Aplysia* pedal ganglion neurons on plasmonic crystal with a neurite (A) and the remnants of the growth cone peripheral region (B). (b) 500–550 nm reflection image of an *Aplysia* pedal ganglion neuron on a plasmonic crystal with a neurite (C) and the remnants of the growth cone peripheral region (D and E). (c) 500–550 nm reflection image of an *Aplysia* pedal ganglion neuron on a plasmonic crystal. “Bulls-eye” structures (denoted with red asterisks) correspond to the central region of the growth cone and are surrounded by thinner “veils” corresponding to the peripheral region of the growth cone. The scale bar in (a) and (b) corresponds to 100 μm , and that in (c) corresponds to 50 μm .

regions at presumably different stages of growth. The structure labeled “A” in Figure 6a (thickness calibrated reflection image using combination of 570–600 nm and 570–1000 nm images) appears to be a neurite which has fully formed. The area labeled “B” appears to be a sparse distribution of thin features and may be the remnants of the peripheral region of the growth cone. Similarly, the darker neurite on the left side (labeled “C”) is readily distinguished from the thinner region (labeled “D”), and the patchy nature of the surface coverage moving further away from the cell body (labeled “E”) may be indicative of the

resorption or partial resorption of the peripheral portion of the growth cone (Figure 6b). The cell structures characterized by “Newton’s ring” in the thin film interference analysis may be the central regions of the growth cones (red asterisks in Figure 6c), which are surrounded by the thin “veil” previously associated with the peripheral region of the growth cone. The neurons in Figure 6a,b have more clearly defined neurites and fewer central regions and thus may be more mature, while the less developed neuron shown in Figure 6c has a morphology characterized by fewer defined neurites and many more growth cone regions.

CONCLUSIONS

We describe a label-free imaging technique that utilizes a plasmonic crystal in conjunction with bandpass filters to quantify the thickness of thin film structures present in a model complex biological structure, pedal ganglion neurons from *Aplysia californica* that were fixed after growth in culture. Contrast calibrations using polyelectrolyte LBL assemblies were applied to estimate the thickness of thin growth regions of the neurons on the plasmonic crystals. The reliability of the imaging method was confirmed with height profiles acquired by AFM. The use of bandpass filters to restrict the wavelengths of light imaged can improve image contrast and sensitivity, with further improvements possible by a combination of images acquired with different bandpass filters. Computational studies provide insight into contrast changes associated with plasmonic phenomena as a function of film thickness. Films having thicknesses beyond the limit of this SPR method can be analyzed using alternative nonplasmonic optical effects, such as Fresnel reflection, scattering, and absorption. Further improvements to the image contrast and sensitivity may be achieved through optimization of the plasmonic crystal structure. This plasmonic reflection imaging method has the potential to be adapted for live cell imaging, because it does not demand the specific operating conditions and long scanning times. While this imaging technique was utilized to analyze the thickness of a fixed cell in this study, this quantitative imaging method shows considerable promise as a noninvasive, sensitive, and cost-effective analytical technique for studying cell morphology with high spatial resolution or cell dynamics stimulated by chemical or physical changes in real time. Studies are in progress to explore these applications.

ASSOCIATED CONTENT

Supporting Information

Schemes of the soft nanoimprint lithography process; SEM image of the plasmonic crystal; comparison of FDTD calculated reflection spectra for pairs of optically equivalent polyelectrolyte and index-corrected thin films; reflection images of *Aplysia* pedal neurons on flat gold surfaces; spectral sensitivity of CCD camera; calculations of film thickness using light interference. This material is available free of charge via the Internet at <http://pubs.acs.org>.

AUTHOR INFORMATION

Corresponding Author

*E-mail: r-nuzzo@illinois.edu.

Author Contributions

[†]These authors contributed equally.

Notes

The authors declare no competing financial interest.

ACKNOWLEDGMENTS

The authors thank Xiying Wang for preparing the *Aplysia* cell cultures. This work was supported by the U.S. Department of Energy under Prime Award No. DE-SC0001293 via Subcontract 67N-1087758 from the California Institute of Technology as part of the DOE Energy Frontier Research Center on Light-Material Interactions in Energy Conversion and was performed using resources at the Frederick Seitz Materials Research Laboratory Central Facilities at the University of Illinois, including the Center for Microanalysis of Materials, the Micro/Nanofabrication Facility, and the Laser and Spectroscopy Facility. We also acknowledge the use of the Turing cluster, maintained and operated by the Computational Science and Engineering Program at the University of Illinois.

REFERENCES

- (1) Barry, R. A.; Shepherd, R. F.; Hanson, J. N.; Nuzzo, R. G.; Wiltzius, P.; Lewis, J. A. Direct-write assembly of 3D hydrogel scaffolds for guided cell growth. *Adv. Mater.* **2009**, *21* (23), 2407–2410.
- (2) Millet, L. J.; Stewart, M. E.; Sweedler, J. V.; Nuzzo, R. G.; Gillette, M. U. Microfluidic devices for culturing primary mammalian neurons at low densities. *Lab Chip* **2007**, *7* (8), 987–994.
- (3) Millet, L. J.; Stewart, M. E.; Nuzzo, R. G.; Gillette, M. U. Guiding neuron development with planar surface gradients of substrate cues deposited using microfluidic devices. *Lab Chip* **2010**, *10* (12), 1525–1535.
- (4) Zhang, H. B.; Shepherd, J. N. H.; Nuzzo, R. G. Microfluidic contact printing: A versatile printing platform for patterning biomolecules on hydrogel substrates. *Soft Matter* **2010**, *6* (10), 2238–2245.
- (5) Shepherd, J. N. H.; Parker, S. T.; Shepherd, R. F.; Gillette, M. U.; Lewis, J. A.; Nuzzo, R. G. 3D microperiodic hydrogel scaffolds for robust neuronal cultures. *Adv. Funct. Mater.* **2011**, *21* (1), 47–54.
- (6) Hanson, J. N.; Motala, M. J.; Heien, M. L.; Gillette, M.; Sweedler, J.; Nuzzo, R. G. Textural guidance cues for controlling process outgrowth of mammalian neurons. *Lab Chip* **2009**, *9* (1), 122–131.
- (7) Corum, L. E.; Eichinger, C. D.; Hsiao, T. W.; Hlady, V. Using microcontact printing of fibrinogen to control surface-induced platelet adhesion and activation. *Langmuir* **2011**, *27* (13), 8316–8322.
- (8) Conn, P. M. *Methods in Enzymology: Imaging and Spectroscopic Analysis of Living Cells: Optical and Spectroscopic Techniques*; Elsevier Science: New York, 2012.
- (9) Barty, A.; Nugent, K. A.; Paganin, D.; Roberts, A. Quantitative optical phase microscopy. *Opt. Lett.* **1998**, *23* (11), 817–819.
- (10) Allen, R. D.; Allen, N. S.; Travis, J. L. Video-enhanced contrast, differential interference contrast (AVEC-DIC) microscopy - A new method capable of analyzing microtubule-related motility in the reticulopodial network of *Allogromia laticollaris*. *Cell Motil. Cytoskeleton* **1981**, *1* (3), 291–302.
- (11) Dodt, H. U.; Ziegler, W. Visualizing unstained neurons in living brain-slices by infrared DIC-video microscopy. *Brain Res.* **1990**, *537* (1–2), 333–336.
- (12) Pluta, M. *Advanced Light Microscopy*; Elsevier: New York, 1988.
- (13) Curtis, A. S. Cell reactions with biomaterials: The microscopies. *Eur. Cells Mater.* **2001**, *1*, 59–65.
- (14) Pauletti, G.; Dandekar, S.; Rong, H.; Ramos, L.; Peng, H.; Seshadri, R.; Slamon, D. J. Assessment of methods for tissue-based detection of the HER-2/neu alteration in human breast cancer: A direct comparison of fluorescence in situ hybridization and immunohistochemistry. *J. Clin. Oncol.* **2000**, *18* (21), 3651–64.
- (15) Giepmans, B. N. G.; Adams, S. R.; Ellisman, M. H.; Tsien, R. Y. Review - The fluorescent toolbox for assessing protein location and function. *Science* **2006**, *312* (5771), 217–224.
- (16) Hu, C. D.; Kerppola, T. K. Simultaneous visualization of multiple protein interactions in living cells using multicolor fluorescence complementation analysis. *Nat. Biotechnol.* **2003**, *21* (5), 539–545.

- (17) Zhang, S. F.; Ma, C.; Chalfie, M. Combinatorial marking of cells and organelles with reconstituted fluorescent proteins. *Cell* **2004**, *119* (1), 137–+.
- (18) Stephens, D. J.; Allan, V. J. Light microscopy techniques for live cell imaging. *Science* **2003**, *300* (5616), 82–86.
- (19) Tanaami, T.; Otsuki, S.; Tomosada, N.; Kosugi, Y.; Shimizu, M.; Ishida, H. High-speed 1-frame/ms scanning confocal microscope with a microlens and Nipkow disks. *Appl. Opt.* **2002**, *41* (22), 4704–4708.
- (20) Nakano, A. Spinning-disk confocal microscopy - A cutting-edge tool for imaging of membrane traffic. *Cell Struct. Funct.* **2002**, *27* (5), 349–355.
- (21) Semwogerere, D.; Weeks, E. R. Confocal microscopy. In *Encyclopedia of Biomaterials and Biomedical Engineering*; Wnek, G. E., Bowlin, G. L., Eds.; Taylor and Francis: New York, 2005; p 3434.
- (22) Marquet, P.; Rappaz, B.; Magistretti, P. J.; Cuche, E.; Emery, Y.; Colomb, T.; Depeursinge, C. Digital holographic microscopy: A noninvasive contrast imaging technique allowing quantitative visualization of living cells with subwavelength axial accuracy. *Opt. Lett.* **2005**, *30* (5), 468–470.
- (23) Wang, Z.; Millet, L.; Mir, M.; Ding, H. F.; Unarunotai, S.; Rogers, J.; Gillette, M. U.; Popescu, G. Spatial light interference microscopy (SLIM). *Opt. Express* **2011**, *19* (2), 1016–1026.
- (24) Rotsch, C.; Radmacher, M. Drug-induced changes of cytoskeletal structure and mechanics in fibroblasts: An atomic force microscopy study. *Biophys. J.* **2000**, *78* (1), 520–535.
- (25) Radmacher, M.; Fritz, M.; Kacher, C. M.; Cleveland, J. P.; Hansma, P. K. Measuring the viscoelastic properties of human platelets with the atomic force microscope. *Biophys. J.* **1996**, *70* (1), 556–567.
- (26) Curtis, M. W.; Russell, B. Micromechanical regulation in cardiac myocytes and fibroblasts: Implications for tissue remodeling. *Pflugers Arch.: Eur. J. Physiol.* **2011**, *462* (1), 105–117.
- (27) Homola, J. Surface plasmon resonance sensors for detection of chemical and biological species. *Chem. Rev.* **2008**, *108* (2), 462–493.
- (28) Stewart, M. E.; Anderton, C. R.; Thompson, L. B.; Maria, J.; Gray, S. K.; Rogers, J. A.; Nuzzo, R. G. Nanostructured plasmonic sensors. *Chem. Rev.* **2008**, *108* (2), 494–521.
- (29) Stewart, M. E.; Mack, N. H.; Malyarchuk, V.; Soares, J. A. N. T.; Lee, T. W.; Gray, S. K.; Nuzzo, R. G.; Rogers, J. A. Quantitative multispectral biosensing and 1D imaging using quasi-3D plasmonic crystals. *Proc. Natl. Acad. Sci. U.S.A.* **2006**, *103* (46), 17143–17148.
- (30) Jung, L. S.; Campbell, C. T.; Chinowsky, T. M.; Mar, M. N.; Yee, S. S. Quantitative interpretation of the response of surface plasmon resonance sensors to adsorbed films. *Langmuir* **1998**, *14* (19), 5636–5648.
- (31) Homola, J.; Yee, S. S.; Gauglitz, G. Surface plasmon resonance sensors: Review. *Sensor Actuators, B* **1999**, *54* (1–2), 3–15.
- (32) Johnsson, B.; Lofas, S.; Lindquist, G. Immobilization of proteins to a carboxymethyl-dextran-modified gold surface for biospecific interaction analysis in surface-plasmon resonance sensors. *Anal. Biochem.* **1991**, *198* (2), 268–277.
- (33) Jonsson, U.; Fagerstam, L.; Ivarsson, B.; Johnsson, B.; Karlsson, R.; Lundh, K.; Lofas, S.; Persson, B.; Roos, H.; Ronnberg, I.; Sjolander, S.; Stenberg, E.; Stahlberg, R.; Urbaniczky, C.; Ostlin, H.; Malmqvist, M. Real-time biospecific interaction analysis using surface-plasmon resonance and a sensor chip technology. *Biotechniques* **1991**, *11* (5), 620–627.
- (34) Anker, J. N.; Hall, W. P.; Lyandres, O.; Shah, N. C.; Zhao, J.; Van Duyne, R. P. Biosensing with plasmonic nanosensors. *Nat. Mater.* **2008**, *7* (6), 442–453.
- (35) Jordan, C. E.; Frutos, A. G.; Thiel, A. J.; Corn, R. M. Surface plasmon resonance imaging measurements of DNA hybridization adsorption and streptavidin/DNA multilayer formation at chemically modified gold surfaces. *Anal. Chem.* **1997**, *69* (24), 4939–4947.
- (36) Aldred, N.; Ekblad, T.; Andersson, O.; Liedberg, B.; Clare, A. S. Real-time quantification of microscale bioadhesion events in situ using imaging surface plasmon resonance (iSPR). *ACS Appl. Mater. Interfaces* **2011**, *3* (6), 2085–2091.
- (37) Moh, K. J.; Yuan, X. C.; Bu, J.; Zhu, S. W.; Gao, B. Z. Surface plasmon resonance imaging of cell-substrate contacts with radially polarized beams. *Opt. Express* **2008**, *16* (25), 20734–20741.
- (38) Wang, W.; Wang, S. P.; Liu, Q.; Wu, J.; Tao, N. J. Mapping Single-Cell-Substrate Interactions by Surface Plasmon Resonance Microscopy. *Langmuir* **2012**, *28* (37), 13373–13379.
- (39) Lee, H. J.; Nedelkov, D.; Corn, R. M. Surface plasmon resonance imaging measurements of antibody arrays for the multiplexed detection of low molecular weight protein biomarkers. *Anal. Chem.* **2006**, *78* (18), 6504–6510.
- (40) Malyarchuk, V.; Stewart, M. E.; Nuzzo, R. G.; Rogers, J. A. Spatially resolved biosensing with a molded plasmonic crystal. *Appl. Phys. Lett.* **2007**, *90* (20), 203113–203115.
- (41) Yao, J. M.; Stewart, M. E.; Maria, J.; Lee, T. W.; Gray, S. K.; Rogers, J. A.; Nuzzo, R. G. Seeing molecules by eye: Surface plasmon resonance imaging at visible wavelengths with high spatial resolution and submonolayer sensitivity. *Angew. Chem., Int. Ed.* **2008**, *47* (27), 5013–5017.
- (42) Stewart, M. E.; Yao, J. M.; Maria, J.; Gray, S. K.; Rogers, J. A.; Nuzzo, R. G. Multispectral thin film biosensing and quantitative imaging using 3D plasmonic crystals. *Anal. Chem.* **2009**, *81* (15), 5980–5989.
- (43) Truong, T. T.; Maria, J.; Yao, J.; Stewart, M. E.; Lee, T. W.; Gray, S. K.; Nuzzo, R. G.; Rogers, J. A. Nanopost plasmonic crystals. *Nanotechnology* **2009**, *20* (43), 434011–434018.
- (44) Maria, J.; Truong, T. T.; Yao, J. M.; Lee, T. W.; Nuzzo, R. G.; Leyffer, S.; Gray, S. K.; Rogers, J. A. Optimization of 3D plasmonic crystal structures for refractive index sensing. *J. Phys. Chem. C* **2009**, *113* (24), 10493–10499.
- (45) Yao, J. M.; Le, A. P.; Schulmerich, M. V.; Maria, J.; Lee, T. W.; Gray, S. K.; Bhargava, R.; Rogers, J. A.; Nuzzo, R. G. Soft embossing of nanoscale optical and plasmonic structures in glass. *ACS Nano* **2011**, *5* (7), 5763–5774.
- (46) Yao, J. M.; Le, A. P.; Gray, S. K.; Moore, J. S.; Rogers, J. A.; Nuzzo, R. G. Functional nanostructured plasmonic materials. *Adv. Mater.* **2010**, *22* (10), 1102–1110.
- (47) Caruso, F.; Niikura, K.; Furlong, D. N.; Okahata, Y. Ultrathin multilayer polyelectrolyte films on gold: Construction and thickness determination 0.1. *Langmuir* **1997**, *13* (13), 3422–3426.
- (48) Voros, J. The density and refractive index of adsorbing protein layers. *Biophys. J.* **2004**, *87* (1), 553–561.
- (49) Benesch, J.; Askendal, A.; Tengvall, P. The determination of thickness and surface mass density of mesothick immunoprecipitate layers by null ellipsometry and protein ¹²⁵Iodine labeling. *J. Colloid Interface Sci.* **2002**, *249* (1), 84–90.
- (50) Ye, X. Y.; Xie, F.; Romanova, E. V.; Rubakhin, S. S.; Sweedler, J. V. Production of nitric oxide within the *Aplysia californica* nervous system. *ACS Chem. Neurosci.* **2010**, *1* (3), 182–193.
- (51) Wang, L. P.; Ota, N.; Romanova, E. V.; Sweedler, J. V. A novel pyridoxal 5'-phosphate-dependent amino acid racemase in the *Aplysia californica* central nervous system. *J. Biol. Chem.* **2011**, *286* (15), 13765–13774.
- (52) Romanova, E. V.; Fosser, K. A.; Rubakhin, S. S.; Nuzzo, R. G.; Sweedler, J. V. Engineering the morphology and electrophysiological parameters of cultured neurons by microfluidic surface patterning. *FASEB J.* **2004**, *18* (9), 1267–1269.
- (53) Romanova, E. V.; Oxley, S. P.; Rubakhin, S. S.; Bohn, P. W.; Sweedler, J. V. Self-assembled monolayers of alkanethiols on gold modulate electrophysiological parameters and cellular morphology of cultured neurons. *Biomaterials* **2006**, *27* (8), 1665–1669.
- (54) Jo, K.; Heien, M. L.; Thompson, L. B.; Zhong, M.; Nuzzo, R. G.; Sweedler, J. V. Mass spectrometric imaging of peptide release from neuronal cells within microfluidic devices. *Lab Chip* **2007**, *7* (11), 1454–1460.
- (55) Leong, F. J. W. M.; Brady, M.; McGee, J. O. Correction of uneven illumination (vignetting) in digital microscopy images. *J. Clin. Pathol.* **2003**, *56* (8), 619–621.
- (56) Sony ICX085AL 2/3-in. Progressive Scan CCD Image Sensor with Square Pixel for B/W Cameras, Datasheet No. E95Z10C73; Sony

Corp., <http://www.alldatasheet.com/datasheet-pdf/pdf/47409/SONY/ICX085AL.html>

(57) Lovell, P.; Moroz, L. L. The largest growth cones in the animal kingdom: An illustrated guide to the dynamics of *Aplysia* neuronal growth in cell culture. *Integr. Comp. Biol.* **2006**, *46* (6), 847–870.

(58) Bamberg, J. R. Introduction to cytoskeletal dynamics and pathfinding of neuronal growth cones. *J. Histochem. Cytochem.* **2003**, *51* (4), 407–409.

(59) Burmeister, D. W.; Goldberg, D. J. Micropruning - The mechanism of turning of *Aplysia* growth cones at substrate borders in vitro. *J. Neurosci.* **1988**, *8* (9), 3151–3159.

(60) Kedem, O.; Vaskevich, A.; Rubinstein, I. Improved sensitivity of localized surface plasmon resonance transducers using reflection measurements. *J. Phys. Chem. Lett.* **2011**, *2* (10), 1223–1226.